Chapter 1

Introduction and literature review

1.1 Motivation for the thesis

Perovskite oxides with the general formula ABO_3 have been recognized for their range of properties, including ferroelectricity, flexoelectricity, ferromagnetism, ferrotoroidicity, etc [28, 29, 30, 31, 32, 33]. Among these, ferroelectricity is widely studied for its applications *viz.,* sensors, actuators, electrical energy storage systems (ELSSs), energy harvesters, memory devices, and many more [34, 35, 36, 37, 38, 39, 40, 41]. Most of the oxide-based perovskites exhibiting high ferroelectric properties are Pb-based *viz.*, Pb(Zr, Ti)O_3, Pb(Mg,Nb)O_3-xPbTiO_3, Pb($Zn_{1/3}Nb_{2/3}$)O_3-PbTiO_3 etc [42, 43, 44, 45, 46, 47]. However, due to toxic nature of Pb, various countries around the world have implemented several laws to limit the use of Pb. For example, European Union enacted legislation in 2002 to restrict the usage of Pb-based materials [48, 49]. This led to the search for Pb-free alternatives [14, 50, 51, 52]. In this search, equimolar composition of potassium sodium niobate ceramics *viz.*, $K_{0.5}Na_{0.5}NbO_3$ (KNN50), and its solid solutions have emerged as promising alternatives [8, 51, 53, 54, 55, 56]. Moreover, compositional engineering has been used to fine-tune the physical properties of these materials, which often lead to structural phenomena like polymorphic phase boundary (PPB), morphotropic phase

boundary (MPB), and relaxor ferroelectricity [53]. These phase boundaries *viz.*, PPB and MPB demonstrate high physical properties due to the coexistence of two ferroelectric phases at long ranges [57, 58]. On the other hand, relaxor ferroelectrics exhibit a high dielectric constant, which has been attributed to chemical heterogeneity (dopants having different ionic radii and oxidation states placed at the same A/B-sites) in the material [5, 59, 60].

Moreover, a recent study by Yang *et al.* [15] discovered morphotropic relaxor boundary (MRB), which exhibits two polar symmetries at short ranges in an average non-polar cubic matrix. The MRB was first discovered in a KNN50-based solid solution *viz.*, (1-*x*)KNN50-*x*$BaTiO_3$ [15]. Moreover, in the vicinity of MRB, significant enhancement in electrostrain and dielectric permittivity was reported [15, 61]. Further, various researchers doped Strontium (Sr) at the A-site in (1-*x*)KNN50-*x*$BaTiO_3$ to enhance the disorder/relaxor behavior in the material [22, 62]. Among various Sr-doped BT compositions, $Ba_{0.9}Sr_{0.1}TiO_3$ (BST10) exhibits maximum dielectric constant [63, 64, 65, 66].

Inspired by the above-mentioned works, the present study aims to explore a morphotropic relaxor boundary in a KNN50-based perovskite system *viz.*, (1-*x*)KNN50-*x*$Ba_{0.9}Sr_{0.1}TiO_3$ (KBST*x*) for $0.00 \leq x \leq 1.00$ using various characterization techniques *viz.*, X-ray/neutron diffraction, Raman scattering, and pair distribution function.

1.2 Overview of ferroelectricity

Ferroelectricity was first observed in 1921 by Joseph Valasek during his dielectric studies on Rochelle salt ($KNaC_4H_4O_6.4H_2O$; sodium potassium tartrate) [67, 68]. Valasek discovered that Rochelle salt exhibits spontaneous polarization, which can be reversed by applying a suitable electric field [67, 68]. He observed that the polarization initially increases with the electric field and follows a characteristic S-shaped hysteresis curve. Moreover, the pioneering work done by Valasek laid the foundation for ferroelectric materials. Further,

discovery of Barium titanate ($BaTiO_3$) in 1940s was a significant milestone because $BaTiO_3$ was the first oxide perovskite (ABO_3-type) exhibiting ferroelectricity. The physical properties of $BaTiO_3$ *viz.*, high dielectric constant and ferroelectricity, and associated structural phase transitions, paved the way for applications of ferroelectricity in capacitors, piezoelectric devices, etc [69].

1.2.1 Characteristics of ferroelectricity and other related phenomena: Piezoelectricity and Pyroelectricity

Ferroelectricity is a property of certain materials that exhibit spontaneous polarization, whose direction can be reversed on the application of suitable electric field [36, 70]. The ferroelectric materials exhibit a unique polarization curve (hysteresis loop), which results from domain wall switching [34, 71]. The polarization of the ferroelectric materials can be modified by changing the magnitude and direction of the applied electric field. The polarization demonstrates a linear behavior at small fields. Moreover, as the field increases, the direction of the domains starts to align in the direction of the applied electric field, resulting in a nonlinear behavior. On further increase in the applied electric field, the polarization reaches a saturation value, which is referred as saturation polarization. Further, as the applied electric field decreases, the domains start to align in the reversed field direction, and as the field is reduced to zero, a non-zero polarization is observed, which is referred to

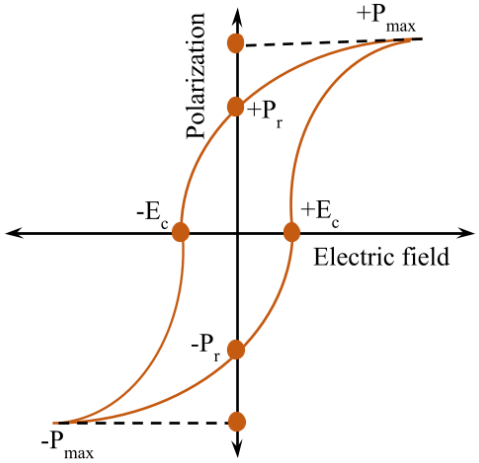

Fig. 1.1 The hysteresis loop illustrates the relationship between polarization and the electric field (P-E) for a typical ferroelectric material. Here, P_r and E_c correspond to remnant polarization and the coercive field, respectively.

as remnant polarization (P_r). In order to reduce the polarization to zero, the field is further increased, and the field at which polarization sets to zero is referred to as the coercive field (E_c). Furthermore, an increase in the field results in polarization saturation in the opposite direction. Once the cycle is completed, a hysteresis loop is achieved, which is shown in Fig. 1.1 [34, 71].

The normal ferroelectric materials obey the Curie-Weiss law above a certain temperature referred to as Curie temperature (T_C). The Curie temperature corresponds to a structural phase transition from a ferroelectric (low symmetry phase) to a paraelectric (high symmetry phase) phase [71]. The above-mentioned Curie-Weiss law is formulated as [34, 36]

$$\varepsilon^{'} = \frac{C}{(T - T_{CW})} \tag{1.1}$$

Here, C represents the Curie constant, and T_{CW} ($T_{CW} \leq T_C$) is the Curie-Weiss temperature.

Ferroelectricity is generally discussed alongside two related phenomena: *viz.,* piezoelectricity and pyroelectricity. Firstly, piezoelectricity refers to the ability of certain materials to generate electric charges when subjected to mechanical stress and vice versa [72, 73]. On the application of mechanical stress, the piezoelectric material deforms and generates an electric charge as an output, and this effect is referred to as the direct piezoelectric effect, which was discovered by Pierre and Jacques Curie in 1880. On the other hand, when the electric field is applied to the piezoelectric material, the material gets strained and the phenomenon is referred to as converse piezoelectric effect (discovered by Gabriel Lippman in 1881) (see Fig. 1.2 and Table 1.1) [74]. Piezoelectricity is characterized

Table 1.1 Types of the Piezoelectric effect

Input	Mechanical Stress	Voltage
Output	Electric charge	Mechanical stress
	Direct Piezoelectric Effect	**Converse Piezoelectric Effect**

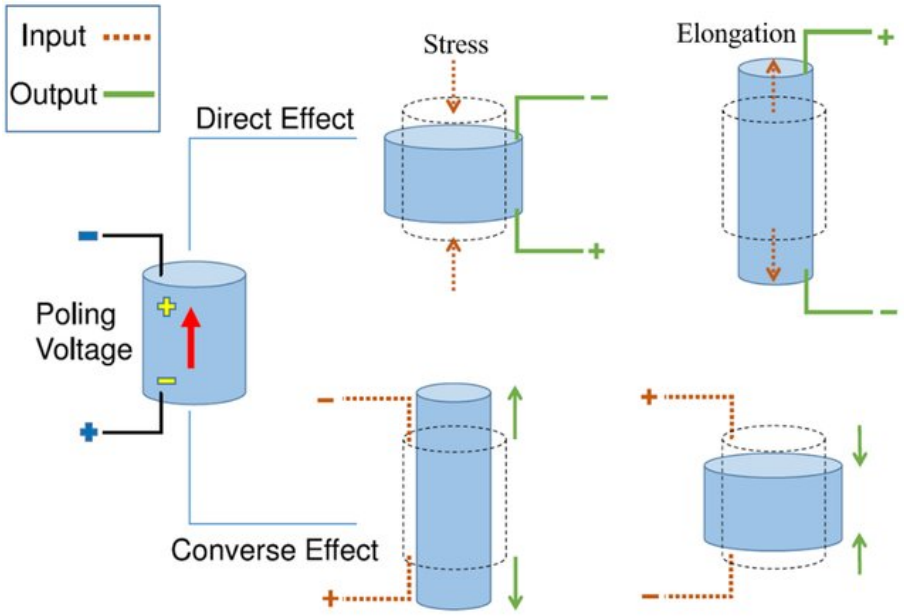

Fig. 1.2 Representation of direct and converse piezoelectric effect [1].

by the piezoelectric coefficient (d), which is defined as the ratio of charge per unit area (polarization) to the applied stress, or alternatively, by the ratio of strain to the electric field [35].

$$P = \frac{Q}{A} = dX \tag{1.2}$$

$$x = dE \tag{1.3}$$

where Q, P, A, X, x, and E represent charge, polarization, area, mechanical stress, strain, and applied electric field, respectively.

Secondly, pyroelectricity is defined as the ability of certain materials (exhibiting non-centrosymmetric structure) to generate electric charge in response to the temperature change [75, 76, 77]. Moreover, on heating the pyroelectric material, the dipoles begin to randomize, thereby decreasing the spontaneous polarization, which results in a current in the external circuit. This current is referred to as pyroelectric current (i_{p}). Conversely, cooling of the pyroelectric material enhances spontaneous polarization, thereby reversing the current [78]. Further, the pyroelectric current (i_{p}) is described by the following equation

[79],

$$i_{\mathrm{p}} = A\left[\frac{dP_{\mathrm{S}}}{dT}\right]\left[\frac{dT}{dt}\right] \tag{1.4}$$

Here, A, $\frac{dP_{\mathrm{S}}}{dT}$, and $\frac{dT}{dt}$ represent the area of the sample, pyroelectric coefficient, and heating rate, respectively [76, 79].

Classification of piezoelectrics, pyroelectrics, and ferroelectrics based on point groups

The above-mentioned phenomena, *viz.,* ferroelectricity, piezoelectricity, and pyroelectricity, are directly linked with the crystal structure of the materials. Crystals are classified into seven distinct crystal systems *viz.*, cubic, tetragonal, hexagonal, rhombohedral, orthorhombic, monoclinic, and triclinic, falling under 32 crystallographic point groups [35]. These 32 point groups are divided into two groups, one with centrosymmetric structures (11 point groups) and the other with non-centrosymmetric structures (21 point groups). Among these, 21 point groups *viz.*, 432, $\overline{4}3m$, 23, 622, $\overline{6}m2$, $\overline{6}$, 422, $\overline{4}2m$, $\overline{4}$, 32, 222, 6*mm*, 6, 4*mm*, 4, 3*m*, 3, *mm*2, 2, m, and 1 are non-centrosymmetric and the remaining 11 point groups *viz.*, *m*3*m*, *m*3, 4/*mmm*, 4/*m*, 6/*mmm*, 6/*m*, $\overline{3}m$, $\overline{3}$, *mmm*, 2/*m*, and $\overline{1}$ are centrosymmetric [35]. Out of 21 non-centrosymmetric point groups, 20 point groups demonstrate piezoelectricity. The non-centrosymmetric point group 432 does not exhibit piezoelectricity because the symmetry operations cancel out polarization [35]. Moreover, out of 20 piezoelectric point groups, there are 10 point groups *viz.*, 6, 6*mm*, 3, 3*m*, 4, 4*mm*, *mm*2, 2, *m*, and 1 that are polar and constitute a class of pyroelectric material [35]. Among these 10 point groups, those point groups in which polarization can be reversed by applying an electric field are classified as ferroelectrics [35, 80]. Consequently, ferroelectric materials exhibit both pyroelectric and piezoelectric properties [14]. Therefore, ferroelectric materials have continually attracted research interest for their scientific and technological importance.

1.3 Perovskite structure (ABO_3)

The term perovskite was coined after the discovery of $CaTiO_3$ in Ural mountains of Russia in 1839 by a German scientist, Gustav Rose [81, 82]. The perovskite material exhibits an ABO_3-type structure where A-site cation is placed at the corner, B-site cation at the body center, and oxygen atoms sit at the face center of the cubic unit cell (see Fig. 1.3). The perovskite materials exhibit various fascinating properties like ferroelectricity, piezoelectricity, flexoelectricity, ferromagnetism, superconductivity, optical properties, etc [83, 84].

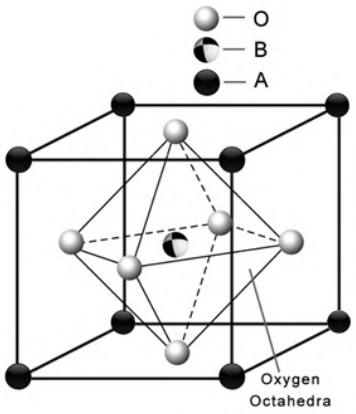

Fig. 1.3 The unit cell of an ideal cubic perovskite (ABO_3) structure.

The diverse range of properties exhibited by perovskites has been attributed to its flexible structure, which can result from the distortions in the simple cubic phase of ideal perovskite (Space Group: $Pm\bar{3}m$) [83, 84]. Moreover, the stability of the perovskite structures is described by Goldschmidt tolerance factor (t), which is given as [24, 85]:

$$t = \frac{r_A + r_B}{\sqrt{2}(r_B + r_O)} \tag{1.5}$$

Here, r_A, r_B, and r_O correspond to the ionic radii of the A-site, B-site, and oxygen atoms, respectively. Based on the magnitude of the tolerance factor (t), the degree of distortion and nature of ordering can be predicted for the perovskite structure (see Table 1.2) [24, 85].

Table 1.2 Different possible structures based on the tolerance factor (t) [23, 24].

t	Structure	Nature of ordering	Example
t = 1	cubic	Paraelectric	$SrTiO_3$, $BaSnO_3$, $BaZrO_3$
$0.78 \leq t \leq 1.07$; excluding t = 1	distorted structures	Antiferroelectric/Paraelectric/ Ferroelectric	$CaZrO_3$, $CaSnO_3$, $CaTiO_3$, $SrZrO_3$, $SrSnO_3$, $NaNbO_3$ $PbZrO_3$, $BaTiO_3$, $KNbO_3$ $PbTiO_3$, $BiFeO_3$

1.3.1 Theories to explain ferroelectricity in perovskite materials

The ferroelectricity in ABO_3 perovskite structures can be explained by various theories (or models) *viz.*, order-disorder model, displacive model/soft mode theory, and hybridization model.

Order-disorder model

According to the order-disorder model, the high-temperature paraelectric phase with cubic structure exhibits off-centering of B-site atoms. As the temperature decreases, the local off-centered B-site atoms undergo a cooperative alignment, resulting in an ordered state at low temperatures [75, 86]. For example, $BaTiO_3$ undergoes a series of long-range structural phase transitions as a function of temperature (T) *viz.*, $R3m \xrightarrow{\approx 183K} Amm2 \xrightarrow{\approx 273K} P4mm \xrightarrow{\approx 393K} Pm\bar{3}m$, whereas Ti atoms are off-centered in all the phases along <111> direction(s) resulting in a short-range order [87]. At high temperatures ($T > 393$ K), the Ti atoms are locally off-centered and can assume eight possible directions, which averages out to give a resultant cubic phase at long ranges [87]. On lowering temperatures (273 K $< T <$ 393 K), the locally off-centered Ti atom can assume four possible directions ($[111]_{pc}$, $[\bar{1}11]_{pc}$, $[1\bar{1}1]_{pc}$, $[\bar{1}\bar{1}1]_{pc}$; pc $\rightarrow$ pseudo cubic), which averages out to give a resultant tetragonal phase ($P4mm$) at long ranges (*i.e.*, $[111]_{pc}$+$[\bar{1}11]_{pc}$+$[1\bar{1}1]_{pc}$+$[\bar{1}\bar{1}1]_{pc}$=$[001]_{pc}$) [87]. Moreover, on further lowering temperatures (183 K $< T <$ 273 K), the locally off-centered Ti atom can assume two possible directions ($[111]_{pc}$, $[\bar{1}11]_{pc}$), which averages out to give a resultant orthorhombic phase ($Amm2$) at long ranges (*i.e.*, $[111]_{pc}$+$[\bar{1}11]_{pc}$=$[011]_{pc}$) [87]. Finally at very low temperatures ($T <$ 183 K), Ti atom assumes one direction ($[111]_{pc}$), resulting in an ordered rhombohedral phase ($R3m$) [87]. Therefore, we see that the symmetry of the local structure is different from that of the average structure for orthorhombic, tetragonal, and cubic phase at long ranges [56, 87]. Similar inferences for long and short ranges can be drawn for $K_{0.5}Na_{0.5}NbO_3$ [56].

Displacive model/Soft mode theory

The displacive model, often interpreted using soft mode theory, explains the evolution of low-symmetry ferroelectric phase (at low temperatures) from a high-symmetry paraelectric phase (at high temperatures) *via* small static displacements. According to this model, a ferroelectric phase transition is driven by the softening/freezing of a specific optical phonon mode associated with the center of the cubic Brillouin zone (q = 0,0,0). Here, softening of phonon modes implies a decrease in frequency on decreasing temperatures, and finally, the frequency becomes zero at Curie temperature (T_C). Consequently, ions are displaced from their centrosymmetric positions, giving rise to net resultant polarization, thereby stabilizing a ferroelectric phase at low temperatures [75, 88]. For instance, various low symmetry ferroelectric phases of $BaTiO_3$ and $K_{0.5}Na_{0.5}NbO_3$ *viz.*, *P*4*mm*, *Amm*2, *R*3*m*, and *Pm* results from the freezing of soft ferroelectric phonon mode (Γ_4^-) associated with the center of the cubic Brillouin zone assuming different order parameter directions (OPD) for different phases (see Table 1.3) [24, 89].

Table 1.3 Different ferroelectric phases obtained after freezing of ferroelectric phonon mode Γ_4^- giving rise to polarization along different directions.

Phase (Space Group)	**Order Parameter Direction (OPD)**
Tetragonal (*P*4*mm*)	P_x=P_y=0, $P_z \neq 0$; (0,0,a)
Orthorhombic (*Amm*2)	P_x=$P_y \neq 0$, P_z=0; (a,a,0)
Rhombohedral (*R*3*m*)	P_x=P_y=$P_z \neq 0$; (a,a,a)
Monoclinic (*Pm*)	$P_x \neq 0$; $P_y \neq 0$; $P_x \neq P_y$; P_z = 0; (a,b,0)

Hybridization model

The stabilization of ferroelectricity in ABO_3 perovskites depends on the balance between the short-range repulsions favoring non-ferroelectric phase, and covalent nature of the bonds favoring ferroelectricity [29, 90]. Moreover, the bonding character (ionic/covalent) in perovskites governs the centrosymmetric/non-centrosymmetric behavior of the unit cell. The centrosymmetric/paraelectric structure is stable in perovskites dominated by ionic bonds, as ionic bonds promote short-range repulsions [91]. The non-

centrosymmetric/ferroelectric structure is stable in perovskites dominated by covalent bonds (driven by hybridization between cation and anion orbitals), as covalent bonds suppress short-range repulsions [92, 93]. Further, the hybridization between B-site cation and surrounding oxygen anions reduces the short-range repulsions, thereby resulting in the displacement of B-site cation from its centrosymmetric position [91, 93]. For example, the origin of ferroelectricity in widely studied ferroelectric materials *viz.*, lead titanate ($PbTiO_3$) and barium titanate ($BaTiO_3$) is also explained by the hybridization between the cations and anions [24, 29]. In $BaTiO_3$, Ba-O bond is ionic in nature, and A-site cation does not significantly contributes to polarization. The ferroelectricity instead originates from the covalent nature of Ti–O bond which results due to the hybridization between Ti ($3d$) and O ($2p$) orbitals. Consequently, Ti cation displaces and results in non-centrosymmetric/ferroelectric structure [24, 29, 94]. However, in $PbTiO_3$, both A- and B-site cations contribute to the ferroelectric nature of the material. Moreover, in $PbTiO_3$, Pb-O bond also exhibits covalent nature which results due to the hybridization between Pb ($6s$) and O ($2p$) orbitals (sp hybridization). Consequently, due to covalent nature, both Ti and Pb atoms displaces from their centrosymmetric position and results in non-centrosymmetric/ferroelectric structure [24, 29, 94]. Therefore, the polar displacements observed in perovskite materials consequently lead to fascinating properties, *viz.,* ferroelectricity, piezoelectricity, pyroelectricity, etc [95, 96].

1.3.2 Soft phonon modes and their role in structural phase transitions

The perovskites (ABO_3) are widely known to undergo structural phase transitions on the application of external stimuli *viz.*, temperature, pressure, electric field, etc [97, 98]. The structural distortions observed in perovskites can be broken up into following components: (i) octahedral tilting (or rotation), (ii) cationic displacements, and (iii) octahedral distortions [97, 99].

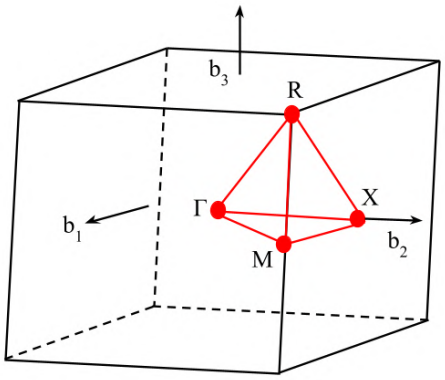

Fig. 1.4 The representation of different points *viz.*, Γ (q = 0,0,0), R (q = $\frac{1}{2}$,$\frac{1}{2}$,$\frac{1}{2}$), M (q = $\frac{1}{2}$,$\frac{1}{2}$,0), and X (q = $\frac{1}{2}$,0,0) in the Brillouin zone of the cubic lattice [2].

These structural distortions can occur separately or in combination, and can be described by the irreducible representation(s) (irreps) of a group corresponding to the soft phonon mode(s) associated with the zone center and (or) zone boundary of the cubic Brillouin zone [100]. In perovskite structures, when an octahedra tilts (or rotates) in a specific way it causes the tilting (or rotation) of neighboring octahedra [24, 99]. Moreover, octahedral tilting (or rotation) are of two types *viz.*, in-phase rotation or positive tilt (denoted by "+" sign) and out-of-phase rotations or negative tilt (denoted by "-" sign) [24, 97, 101]. The in-phase rotations (positive tilt) of the octahedra are observed when the adjacent octahedra rotate in a similar direction along the tilt axis. On the other hand, out-of-phase rotations (negative tilt) of the octahedra are observed when the adjacent octahedra rotate in opposite directions along the tilt axis. Further, octahedral rotations are associated with the zone boundary of the cubic Brillouin zone and are responsible for antiferrodistortive phase transitions *i.e.*, the unit cell of low symmetry (low temperatures) phase is multipled with respect to high symmetry (high temperature) cubic phase (Space Group: $Pm\bar{3}m$). Moreover, in-phase rotations (or positive tilts) result from the freezing of soft phonon mode (M_3^+ irrep of a group) associated with the M-point (q = $\frac{1}{2}$,$\frac{1}{2}$,0) of the cubic Brillouin zone (see Fig. 1.4), whereas out-of-phase rotations (or negative tilts) result from the freezing of soft phonon mode (R_4^+ irrep of a group) associated with the R-point (q = $\frac{1}{2}$,$\frac{1}{2}$,$\frac{1}{2}$) of the cubic Brillouin zone (see Fig. 1.4) [24, 97, 100, 102].

Furthermore, other types of structural distortions *viz.*, cation displacements and octahedral distortions are usually associated with each other [97, 98, 99, 103]. These structural

distortions result from the freezing of soft phonon mode(s) associated with the zone boundary ($q \neq 0$) and (or) zone center ($q = 0$) of the cubic Brillouin zone (see Fig. 1.4) [24, 100, 102, 104]. The cation displacements can be parallel or anti-parallel, consequently resulting in ferroelectric structure or antiferroelectric structure, respectively [97, 99]. For example, the low symmetry phases of $BaTiO_3$/$KNbO_3$ *viz.*, *P*4*mm*, *Amm*2, and *R*3*m* exhibit parallel displacements of B-site cations along different directions. These parallel displacements of B-site cations result from the freezing of Γ_4^- (q = 0,0,0) phonon mode along different OPDs [24, 89]. On the other hand, the antiferroelectric phase of $NaNbO_3$ (Space Group: *Pbcm*) exhibits antiparallel displacements of ions, resulting from the freezing of Δ_5 ($q = 0,0,\frac{1}{4}$) soft phonon mode associated with cubic Brillouin zone [105, 106].

Therefore, soft phonon mode(s) play a crucial role in explaining ferrodistortive (associated with zone centre of cubic Brillouin zone) and (or) antiferrodistortive (associated with zone boundary of cubic Brillouin zone) structural phase transitions which results in high physical properties *viz.*, ferroelectricity, piezoelectricity, non-linear optical properties, etc at critical temperatures [24, 98, 102].

1.4 Compositional Engineering

The first ferroelectric perovskite *viz.*, Barium titanate ($BaTiO_3$) exhibits fascinating physical properties like ferroelectricity, piezoelectricity, pyroelectricity, electrocaloric effect, etc [30, 107, 108, 109, 110]. However, its performance remains significantly lower in comparison to Pb-based perovskites like $PbTiO_3$, $Pb(Zr_xTi_{(1-x)})O_3$ (PZT), (1-x)Pb(Mg, Nb)O_3-$x$$PbTiO_3$, etc. In order to enhance the physical properties of $BaTiO_3$, researchers have used various methods such as chemical substitutions [7, 104, 111], grain size engineering [112], high-pressure treatment [113], etc. Among various methods, chemical substitution (or doping) has emerged as an effective way in tuning physical properties *viz.*, ferroelectricity, dielectric constant, piezoelectricity etc., at ambient conditions [7, 104, 111, 114]. The

strategic substitution at A/B sites in ABO_3 perovskites may result in the stabilization of highly responsive phase coexistence regions. These phase coexistence regions are primarily referred as polymorphic phase boundary (PPB) or morphotropic phase boundary (MPB) [58, 115]. The presence of these phase boundaries play a crucial role in tuning the physical properties of perovskite based materials for advanced applications [14, 57]. On the other hand, the substitutions with high mismatch in ionic radii and (or) different oxidation states, induces local strains/fields, resulting in disordered/relaxor ferroelectric systems. The disordered/relaxor ferroelectric systems are characterized by diffused phase transitions, frequency dispersion, and enhanced dielectric constant [7, 116, 117, 118].

1.4.1 Polymorphic phase boundary (PPB) and Morphotropic phase boundary (MPB)

The idea of phase coexistence involves two types of phase boundaries *viz.*, polymorphic phase boundary (PPB) (temperature-driven) and morphotropic phase boundary (MPB) (composition-driven). The polymorphic phase boundary (PPB) exhibits coexistence of two ferroelectric phases having strong temperature dependence (see Fig. 1.5). On the other hand, morphotropic phase boundary (MPB) exhibits coexistence of two ferroelectric phases having weak temperature dependence (see Fig. 1.5) [14, 57]. Moreover, the physical properties *viz.*, piezoelectricity, ferroelectricity, etc., enhances in the vicinity of PPB/MPB [54, 58, 119]. This enhancement in the physical properties has been attributed to the polarization rotation and (or) polarization extension phenomenon [58]. These phenomenon arise due to the flattening of the free energy profile, allowing easy switching between the polarization states [57, 58, 120, 120]. The polarization rotation phenomenon occurs in ferroelectric to ferroelectric phase transitions, and the polarization extension phenomenon occurs in paraelectric to ferroelectric phase transitions [58, 121].

Further, the flattening of the free energy profile is observed in the vicinity of PPB and facilitates the polarization rotation/extension phenomenon, thereby resulting in high physical properties [122]. Moreover, PPBs exhibit strong temperature dependence, thereby limiting their applications in devices requiring thermal stability.

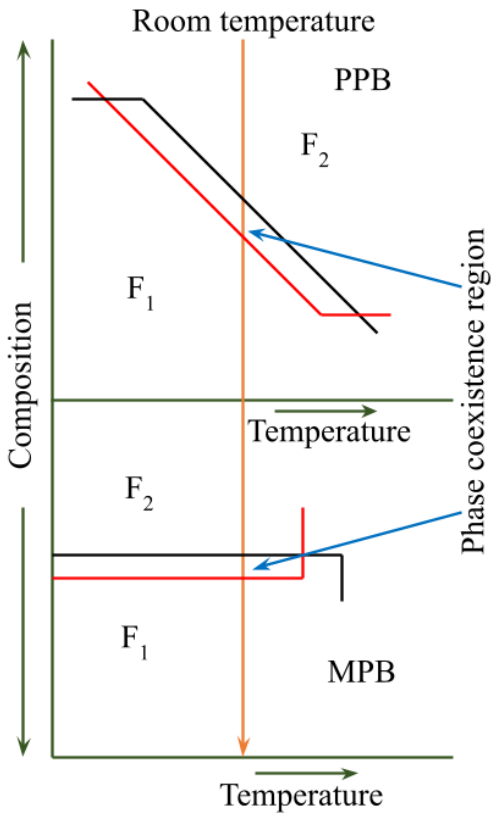

Fig. 1.5 Representation of polymorphic phase boundary (PPB) and morphotropic phase boundary (MPB) existing between two ferroelectric phases *viz.*, F_1 and F_2.

On the other hand, MPBs demonstrate high physical properties (due to polarization rotation and polarization extension phenomenon) with weak temperature dependence (see Fig. 1.5), and are thermally stable, thereby making them suitable for devices demanding thermal stability. Most of the widely studied MPBs are Pb-based *viz.*, $Pb(Ti_xZr_{(1-x)})O_3$ (PZT) [53, 123], $Pb(Mg_{1/3}Nb_{2/3})O_3$-$PbTiO_3$ [124, 125], $Pb(Zn_{1/3}Nb_{2/3})O_3$-$PbTiO_3$ [46, 47], etc. Among these, PZT is a well-known Pb-based material with MPB lying between $0.48 \leq Ti(x) \leq 0.50$ (see Fig. 1.6) [53, 123]. Here, MPB exhibits coexistence of two ferroelectric phases *viz.*, tetragonal (Space Group: *P*4*mm*) and rhombohedral (Space Group: *R*3*m*) for a wide temperature range (see Fig. 1.6) [53, 123]. The physical properties *viz.*, piezoelectric constant, electromechanical coupling coefficients, etc., gets maximized in the vicinity of MPB for PZT [123]. Moreover, Noheda *et al.* in 1999, reported monoclinic phase with *Cm* space group for MPB composition of PZT [123]. The monoclinic phase with *Cm* space group is a subgroup of *P*4*mm* and *R*3*m* phase, and acts as a bridging phase between the two ferroelectric phases [43, 123]. Subsequently, the monoclinic phase provides an easy

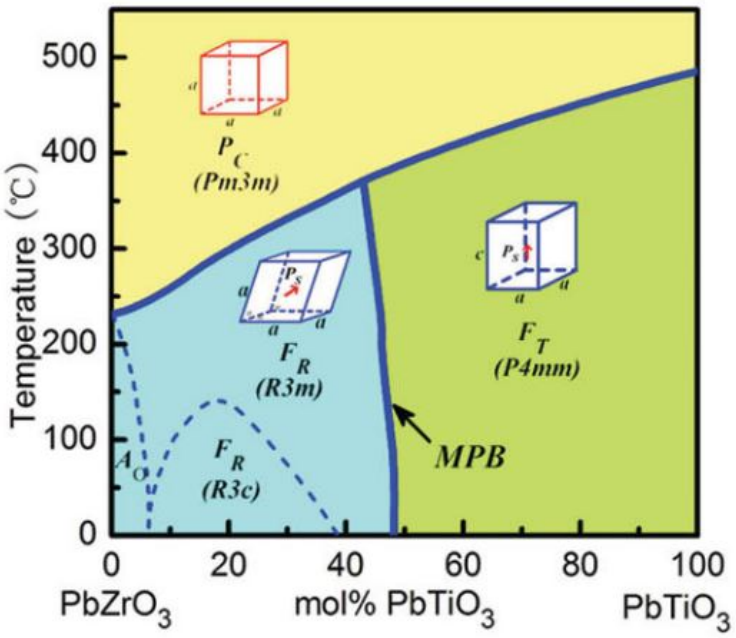

Fig. 1.6 Morphotropic phase boundary in $Pb(Zr,Ti)O_3$ (PZT) ceramics [3].

path for polarization rotation, which consequently results in high physical properties of PZT [43, 58, 123].

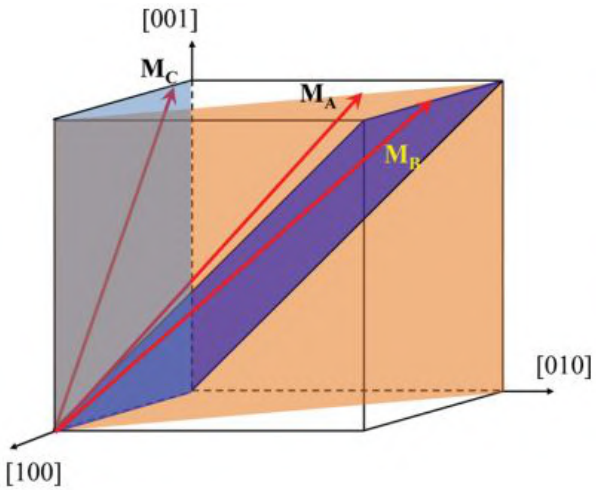

Fig. 1.7 Schematic representation of polar directions in monoclinic M_A, M_B, and M_c phases [4].

Further, various authors have reported different types of monoclinic phases *viz.*, M_A, M_B, and M_c, which correspond to *Cm*, *Cm*, and *Pm* space groups, respectively [43, 123,

126, 127, 128]. Although M_A and M_B type monoclinic phases are associated with the same space group, they possess different polarization equations, resulting from the differences in magnitude and directions of cationic displacements (see Table 1.4) [127, 129]. For M_A phase, $P_x = P_y < P_z$, whereas for M_B phase, $P_x = P_y > P_z$ (see Table 1.4) [44, 126, 129].

Table 1.4 Type of monoclinic phases with different polarization configuration and cation displacements. Here, R, O, and T represent rhombohedral, orthorhombic, and tetragonal phases, respectively.

Type of Monoclinic phase	polarization configuration	Cation displacements
M_A	$P_x = P_y < P_z$	<111> (R) and <100> (T)
M_B	$P_x = P_y > P_z$	<111> (R) and <110> (O)
M_C	$P_x \neq 0$; $P_y \neq 0$; $P_x \neq P_y$; $P_z = 0$	<110> (O) and <100> (T)

Furthermore, Damjanovic *et a*l. demonstrated that both polarization rotation and polarization extension are responsible for high physical properties (at triple point) at high temperatures for PZT (see Fig. 1.6) [58].

Now, in addition to PPB and MPB-based ferroelectric systems, where two distinct phases are stable at long ranges, there is another class of materials observed in dielectrics, where two distinct phases are stable at long and short ranges. This fascinating class of materials is popularly known as relaxor ferroelectrics [130].

1.4.2 Relaxor ferroelectrics

The history of relaxor ferroelectrics (or relaxors) dates back to 1960s with the discovery of unusual dielectric behavior in Pb-based perovskite solid solution *viz.*, $Pb(Mg,Nb)O_3$ (PMN) by Smolenskii and Agranovskaya in Soviet Union [131]. They observed that PMN exhibits a broad temperature-dependent dielectric peak, unlike normal ferroelectrics. This led to the discovery of a new class of ferroelectric materials, later termed as relaxor ferroelectrics by L.E. Cross in 1987 [5, 59, 132, 133]. Relaxor ferroelectrics have gained significant attention due to their unique structural configuration and wide range

of scientific and technological applications. They exhibit high dielectric constant and excellent electromechanical properties stable for a wide temperature range, making them useful for sensors, actuators, energy storage devices, electrocaloric cooling, electrostrictive applications etc [5, 117, 130, 134, 135, 136].

Definition and characteristics

Relaxor ferroelectrics are materials with unique structure and exceptional physical properties [5]. Moreover, relaxor behavior in perovskites (ABO_3) has been attributed to chemical heterogeneity *i.e.*, large differences in ionic radii, and/or different oxidation states of the dopants [5, 7]. Further, in 1987, Cross stated three features defining a relaxor material:

1. Temperature-dependent dielectric data of a relaxor material exhibits a broad and smeared maximum (see Fig. 1.8),

2. Temperature corresponding to dielectric maxima *viz.*, T_m must exhibit a frequency dispersion *i.e.*, T_m shifts towards higher temperature with increasing frequency (see Fig. 1.8), and

3. The macroscopic symmetry should not break under thermal variations [5, 59, 137].

The macroscopic symmetry in most of the relaxor ferroelectrics is cubic with $Pm\bar{3}m$ space group. It is well known that materials exhibiting cubic symmetry lack polarization, and a linear behavior is observed in P-E measurements of the materials. However, despite having a non-polar cubic symmetry, a non-linear, slim hysteresis (P-E) loop is observed for relaxor ferroelectrics (see Fig. 1.9). This contradictory nature has been explained by the presence of polar nanoregions (PNRs) (typically 2-10 nm in size) in an average cubic matrix (see Fig. 1.10). Moreover, the interaction among the PNRs has been held responsible for the slim hysteresis loop observed in relaxor materials [5, 7, 118, 137].

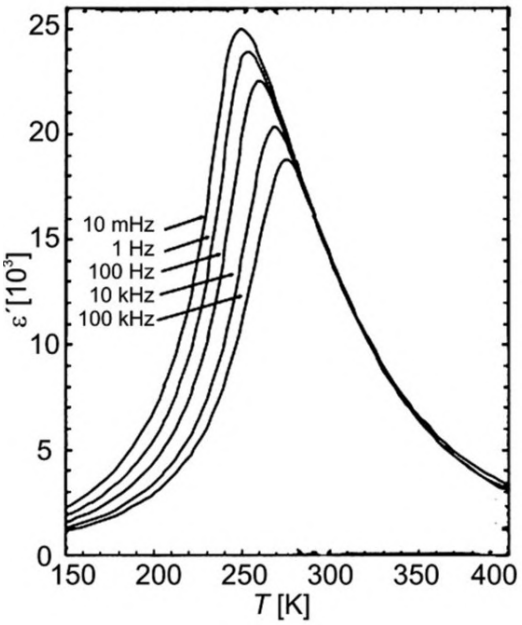

Fig. 1.8 The figure represents the frequency-dependent real part of the dielectric constant of relaxor ferroelectric *viz.*, Pb(Mg, Nb)O_3 [5].

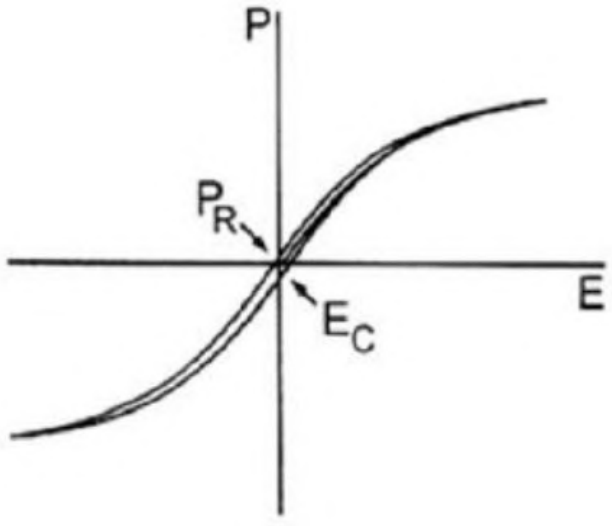

Fig. 1.9 Slim P-E loop observed for a relaxor ferroelectrics [6, 7]. Here, P_R and E_C correspond to remnant polarization and coercive field, respectively.

Further, relaxor ferroelectrics exhibit various characteristic temperatures *viz.*, Burns temperature (T_B) [138], intermediate temperature (T^*) [139, 140, 141], temperature corresponding to dielectric maximum (T_m), and Vogel-Fulcher freezing temperature (T_{VF})

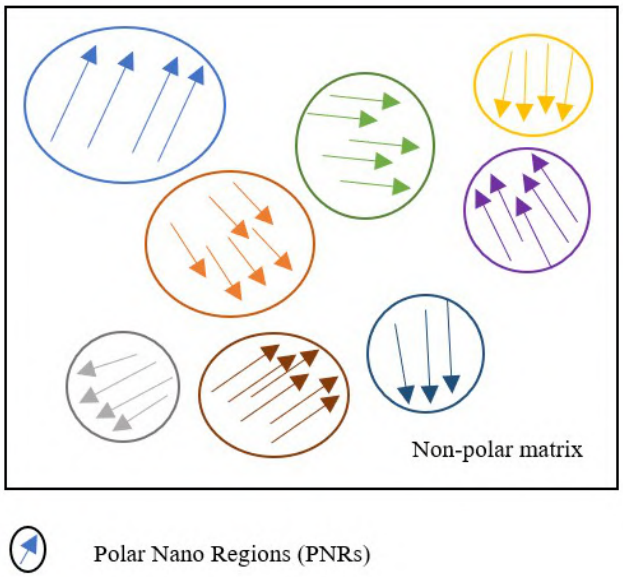

Fig. 1.10 Schematic representation of polar nanoregions in the non-polar (cubic) matrix.

[5, 7, 118, 137]. A paraelectric cubic phase is stable above T_B, where no correlations are observed among fluctuating electric dipoles [25]. On cooling below T_B, the nucleation and growth of polar clusters (PNRs) (displaying dynamic behavior) and their interactions (intra/inter) begin [25, 142]. Subsequently, a static component in PNRs starts to develop (*i.e.*, the dynamics of PNRs begin to slow down) below a certain temperature, referred to as intermediate temperature (T^*) [139, 140, 141]. Moreover, the dielectric constant maximizes at a temperature (T_m) [59, 142]. On cooling below T_m, the dynamics of PNRs further slow down and finally freeze below a certain temperature referred to as Vogel-Fulcher freezing temperature (T_{VF}) [5, 7, 137, 143]. Based on the above discussions, the relaxor ferroelectrics exhibit four phases *viz.*, the paraelectric phase ($T > T_B$), the (quasi)dynamic-relaxor phase ($T^* < T < T_B$), the (quasi)static-relaxor phase ($T_{VF} < T < T^*$), and the frozen phase ($T < T_{VF}$) (see Table 1.5) [25, 26].

Owing to the broad and diffused nature of dielectric permittivity, the relaxor ferroelectrics do not follow Curie-Weiss law (see equation 1.1) below T_B (the temperature below which PNRs nucleate and start to grow) [5]. Moreover, Uchino proposed a modified

Table 1.5 Various phases exhibited by relaxor ferroelectrics as a function of temperature [25, 26].

Temperature range	**Behavior**	**Phase**
$T > \mathrm{T_B}$	No polar correlations	Paraelectric phase
$\mathrm{T^*} < T < \mathrm{T_B}$	Dynamic correlations and No dispersion	(Quasi)dynamic-relaxor phase
$\mathrm{T_{VF}} < T < \mathrm{T^*}$	Dynamic + static correlations and strong dispersion	(Quasi)static-relaxor phase
$T < \mathrm{T_{VF}}$	Static correlations and weak dispersion	Frozen phase

Curie-Weiss law given as [144]:

$$\frac{1}{\varepsilon'} - \frac{1}{\varepsilon'_{\mathrm{m}}} = \frac{(T - T_{\mathrm{m}})^{\gamma}}{C}; T > T_{\mathrm{m}} \tag{1.6}$$

to describe the behavior of relaxor ferroelectric. Here, ε', $\varepsilon'_{\mathrm{m}}$ correspond to the real part of the dielectric constant at temperature T and $\mathrm{T_m}$, respectively, and γ is called the diffusion exponent, whose value lies between $1 \leq \gamma \leq 2$. $\gamma = 1$ corresponds to normal ferroelectric behavior, whereas $\gamma = 2$ corresponds to relaxor ferroelectric behavior [7, 145, 146]. As discussed above, the dynamics of PNRs freeze below Vogel-Fulcher freezing temperature ($\mathrm{T_{VF}}$), and is described by Vogel-Fulcher relation given as [143]:

$$f = f_0 exp\left[\frac{-E_{\mathrm{a}}}{k_{\mathrm{B}}(T_{\mathrm{m}} - T_{\mathrm{VF}})}\right] \tag{1.7}$$

Here, f and $\mathrm{f_0}$ are measured frequency and pre-exponential factor, respectively; $\mathrm{E_a}$ is activation energy, $\mathrm{k_B}$ is Boltzmann constant, $\mathrm{T_m}$ is the temperature corresponding to dielectric maxima, and $\mathrm{T_{VF}}$ is the Vogel-Fulcher freezing temperature.

Thus, we see that relaxor ferroelectrics enjoy a unique structural configuration associated with fascinating physical properties, making them a subject of continuous research, important from a scientific and technological point of view. However, the underlying physics governing relaxor behavior is not fully understood. Further, in order to explain the

underlying physics of relaxor ferroelectrics, various models *viz.*, (i). Diffuse phase transition model, (ii). Superparaelectric model, (iii). Dipolar glass model, and (iv). Random field model have been proposed, and are discussed in the upcoming section.

Diffuse Phase Transition Model

The diffuse phase transition (DPT) model was proposed by Smolenskii, and it was among the earliest attempts made to explain the unique dielectric behavior of relaxor ferroelectrics [147]. According to this model, the relaxor behavior is due to compositional fluctuations *i.e.*, dopants with considerable differences in ionic radii, and (or) different oxidation states, for *e.g.*, $Pb(Mg_{1/3}Nb_{2/3})O_3$ (PMN), $Pb(Sc_{0.5}Ta_{0.5})O_3$ (PST) etc [26, 137]. Here, cations with different ionic radii, and oxidation states *viz.*, Mg^{2+} ($r_{Mg^{2+}}$ = 72 pm) & Nb^{5+} ($r_{Nb^{5+}}$ = 64 pm) and Sc^{3+} ($r_{Sc^{3+}}$ = 74.5 pm) & Ta^{5+} ($r_{Ta^{5+}}$ = 64 pm) are placed at the B-site, resulting in compositional fluctuations [148]. This inhomogeneity develops spatial fluctuations, thereby resulting in the distribution of local Curie temperature corresponding to different micro-regions. Consequently, different micro-regions undergo transition at different temperatures, thereby resulting in a broad and smeared dielectric peak at the macroscopic level [137, 147]. Further, this model explains the role of compositional disorder in explaining unique dielectric behavior demonstrated by relaxor ferroelectrics [137]. However, the DPT model did not explain the frequency dispersion observed in relaxor ferroelectrics [137].

Superparaelectric Model

Building upon the idea of the Diffuse Phase Transition (DPT) Model, L.E. Cross proposed Superparaelectric Model to explain the relaxor behavior. This model suggests that the relaxor ferroelectrics exhibit polar clusters (or polar nanoregions; PNRs) of different sizes and symmetry (*i.e.*, microscopic symmetry) lower than that of macroscopic symmetry.

Moreover, Cross proposed that PNRs become thermally unstable as their volume shrinks, leading to superparaelectric behavior (analogous to superparamagnetism). In this state, the PNRs are highly dynamic and their polarization vector is constantly flipping in equivalent directions above the temperature corresponding to the dielectric maximum (T_m) [137]. Moreover, Cross compared the polarization (P) obtained from dielectric hysteresis measurements with root-mean-square polarization ($\sqrt{P^2}$) obtained from thermal expansion measurements. He observed that although the polarization (P) vanishes above T_m, the root-mean-square polarization ($\sqrt{P^2}$) does not vanish even till a few hundred degrees above T_m, thereby confirming the dynamic behavior of PNRs above T_m. Further, there are a few shortcomings in the superparaelectric model [137]:

1. The superparaelectric model explains the behavior of PNRs above T_m but does not explores the low temperature region ($T < T_m$).

2. The superparaelectric model remains silent over the frequency dispersion characteristic of relaxor ferroelectrics.

Dipolar Glass Model

The dipolar glass model was proposed by Viehland *et al.* to explain the characteristics of relaxor ferroelectrics at low temperatures. The dipolar glass model draws an analogy between relaxor ferroelectrics and spin glass, by proposing that PNRs gradually freeze on decreasing temperatures (similar to spin glass behavior) [143, 149]. Further, relaxational behavior of PNRs in well-known relaxor material *viz.*, PMN was modeled using Arrhenius equation. However, Arrhenius equation gave unreasonable values of activation energy (7 eV) and pre-exponential factor (10^{40} Hz), making it unsuitable for PMN. Owing to unreasonable values obtained from Arrhenius equation, Viehland *et al.* used the Vogel-Fulcher relationship (see equation 1.7) to model the relaxational behavior of PNRs. The Vogel-Fulcher relation gave reasonable values of activation energy (0.0786 eV) and pre-

exponential factor (10^{12} Hz) for PMN, thereby confirming the suitability of Vogel-Fulcher relation for explaining relaxor behavior.

Moreover, the Vogel-Fulcher freezing temperature (T_{VF}) plays a crucial role in governing the dielectric, ferroelectric, and piezoelectric properties of relaxors. Further, two key states of relaxor ferroelectrics are observed around Vogel-Fulcher freezing temperature (T_{VF}) *i.e.*, for $T > T_{VF}$ and $T < T_{VF}$. Firstly, for $T > T_{VF}$, the relaxor ferroelectrics remain in an ergodic state, where PNRs exhibit dynamic behavior, and secondly, for $T < T_{VF}$, the relaxor ferroelectrics enter in a nonergodic state, where PNRs become static. Furthermore, this non-ergodic state can be transformed to a long-range ferroelectric state by applying a suitable electric field [137, 143, 149].

Random Field Model

The Random Field Model was proposed by Westphal, Kleemann, and Glinchuk [150]. According to this model, the chemical disorder in ABO_3 perovskites induces quenched random fields at short ranges, thereby disrupting the formation of a ferroelectric state at long ranges. Consequently, short-range ordered regions with polarization (PNRs) are developed in the material. One of the key achievements of the Random Field Model was its ability to explain the relaxor behavior of systems originating from isovalent substitutions, for *e.g.*, Ba(Sn,Ti)O_3 and Ba(Zr,Ti)O_3, where the B-site cations are substituted with isovalent elements exhibiting considerable difference in ionic radii ($Sn^{4+} \rightarrow 69$ pm and $Ti^{4+} \rightarrow 60.5$ pm; $Zr^{4+} \rightarrow 72$ pm and $Ti^{4+} \rightarrow 60.5$ pm) [148]. This kind was different from relaxors originating from heterovalent substitutions (for *e.g.*, PMN and PST) where charge disorder was held responsible for inducing relaxor behavior. Moreover, isovalent substitutions with large differences in ionic radii creates a non-ferroelectric environment in the ferroelectric matrix, thereby resulting in the relaxor behavior. For instance, in Ba(Sn,Ti)O_3, the incorporation of $BaSnO_3$ (a paraelectric phase with cubic structure) in $BaTiO_3$ (a

ferroelectric phase with tetragonal structure) disrupts the long-range ferroelectric order in $BaTiO_3$, thereby leading to relaxor behavior. Similar behavior is observed for Ba(Zr, Ti)O_3. Further, the isovalent substitution with large differences in ionic radii results in the distortion of TiO_6 octahedra, thereby creating random local strain resulting in ferroelastic domain states. Furthermore, the Random Field Model broadens the understanding of relaxor ferroelectrics by demonstrating that relaxor behavior can be induced by charge disorder (*via* heterovalent substitution) and (or) strain disorder (*via* isovalent substitution with considerable difference in ionic radii) independently or collaboratively [137, 150].

Apart from the above-mentioned models, several other models have been proposed to explain the behavior of relaxor ferroelectrics. These include the Spherical Random-Bond–Random-Field Model [151], Bi-Relaxation Model [137, 152], etc. These models provide additional insights into the complex nature of relaxor ferroelectrics.

Finally, our discussions on compositional engineering highlight that the key phenomena responsible for enhancing the physical properties are structure-driven *viz.*, polymorphic/morphotropic phase boundary (PPB/MPB), and relaxor behavior. Most of the materials exhibiting high physical properties are Pb-based. However, due to the toxic and hazardous nature of Pb, significant research efforts have been made to develop Pb-free alternatives [48, 49, 50, 51]. Among various Pb-free alternatives, $BaTiO_3$ and its solid solutions have emerged as promising candidates. Moreover, $K_{0.5}Na_{0.5}NbO_3$ (KNN50)-based materials have also gained impetus as another potential Pb-free alternative. Various KNN50-based solid solutions such as (K,Na,Ba)(Ti,Nb)O_3, (K,Na,Ba,Sr)(Ti,Nb)O_3, Li modified KNN50, etc. exhibit PPB/MPB and relaxor-like characteristics. Furthermore, we will discuss the structure and associated physical properties of these Pb-free perovskite materials in the upcoming section.

1.5 Literature review on some Pb-free functional materials

1.5.1 $KNbO_3$

Potassium niobate ($KNbO_3$) has been widely studied for its physical properties *viz.*, ferroelectricity, piezoelectricity, optical properties etc., [9, 153]. Shirane *et al.* in 1953 anlaysed temperature-dependent dielectric data and powder photographs of $KNbO_3$, and found that $KNbO_3$ undergoes three successive structural phase transitions on heating *viz.*, Rhombohedral $\xrightarrow{\approx 218K}$ Orthorhombic $\xrightarrow{\approx 473K}$ Tetragonal $\xrightarrow{\approx 683K}$ Cubic (see Fig. 1.11) [8]. Moreover, A.W. Hewat in 1973 performed neutron diffraction measurements and Rietveld refinements to confirm the series of structural phase transitions *viz.*, $R3m \xrightarrow{\approx 263K} Amm2 \xrightarrow{\approx 498K} P4mm \xrightarrow{\approx 708K} Pm\bar{3}m$ [154]. Above-mentioned structural phase transitions were further corroborated by Skjaervo *et al.* [155]. Further, Buixaderas *et al.* reported similar

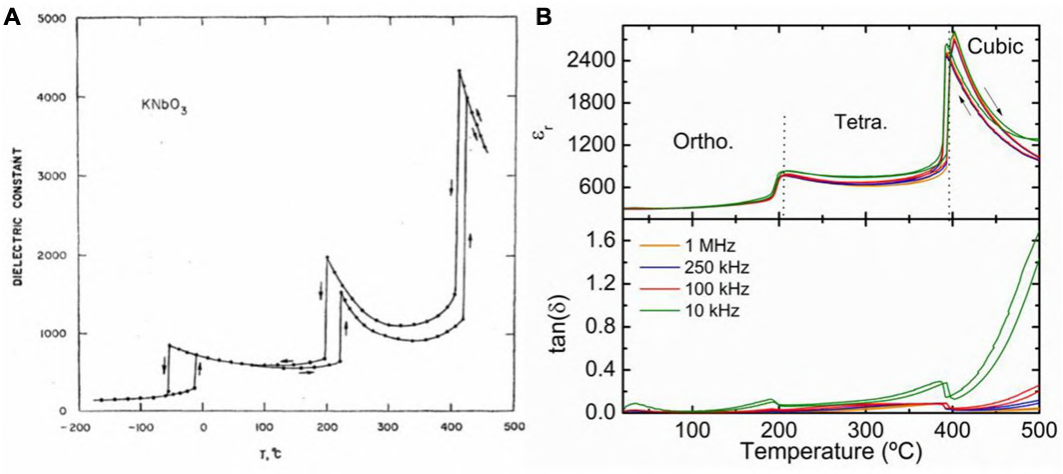

Fig. 1.11 (A) Temperature-dependent evolution of dielectric constant for $KNbO_3$ single crystal [8, 9], and (B) Temperature-dependent evolution of dielectric constant and loss for $KNbO_3$ ceramics [9, 10].

structural phase transitions *i.e.*, Rhombohedral $\xrightarrow{\approx 200K}$ Orthorhombic $\xrightarrow{\approx 510K}$ Tetragonal $\xrightarrow{\approx 755K}$ Cubic for $KNbO_3$ using temperature-dependent Raman scattering data [156].

Furthermore, Kawamura *et al.* performed Synchrotron X-ray diffraction (SXRD) measurement to analyze the electronic charge density of $KNbO_3$ [157]. Kawamura *et al.* used maximum entropy method (MEM), and demonstrated that K ions contribute minimally to electronic polarization, and Nb–O bonds contribute maximally to electronic polarization due to their covalent nature [157].

1.5.2 $NaNbO_3$

Sodium niobate ($NaNbO_3$) is a Pb-free perovskite material that has attracted significant attention due to complex crystal structures and the presence of all the three orders *viz.*, ferroelectric, antiferroelectric, and paraelectric as a function of temperature. Owing to eco-friendly nature, $NaNbO_3$ and its solid solutions have been widely studied for decades as a potential alternative to Pb-based materials, exhibiting a wide range of applications in capacitors, sensors, actuators, energy harvesters, non-linear optical devices, etc [11, 27, 158, 159, 160]. In 1951, C. Kittel suggested the existence of the antiferroelectric state in $NaNbO_3$ [158]. Moreover, in 1974, Helen D. Megaw reported seven crystal structures as a function of temperature for $NaNbO_3$ *viz.*, $F3c$ (N phase) $\xrightarrow{\approx 173K}$ $Pbcm$ (P phase) $\xrightarrow{\approx 633K}$ $Pnmm$ (R phase) $\xrightarrow{\approx 753K}$ $Pnmm$ (S phase) $\xrightarrow{\approx 793K}$ $Ccmm$ (T_1 phase) $\xrightarrow{\approx 848K}$

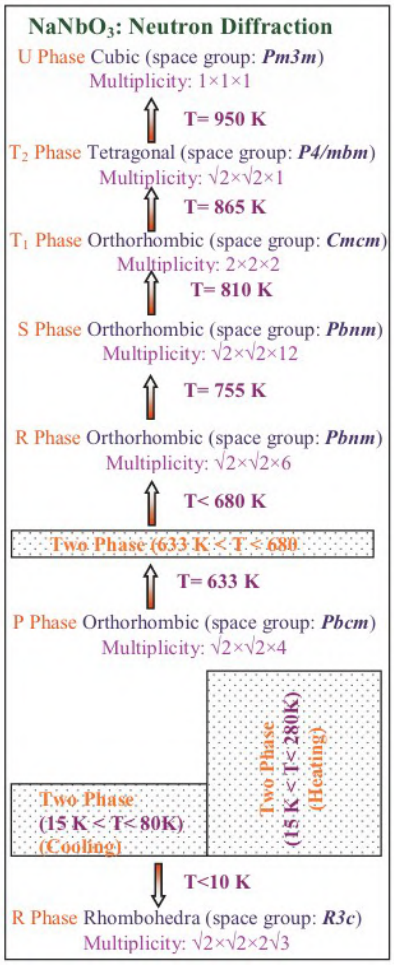

Fig. 1.12 Temperature-dependent phase evolution of $NaNbO_3$ reported by Mishra *et al.* [11].

$F4/mmb$ (T_2 phase) $\xrightarrow{\approx 913K}$ $Pm\bar{3}m$ [159] . Here, the two orthorhombic phases *viz.*, *R* and *S* phases with same space groups *i.e.*, *Pnmm* differs in cell size [159]. At room temperatures $NaNbO_3$ exhibits an orthorhombic structure (Space Group: *Pbcm*) with cell size: $\sqrt{2}a_p \times \sqrt{2}b_p \times 4c_p$, and having a compound tilt system *i.e.*, $(a^-a^-c^+)_1^2(a^-a^-c^-)_2^3(a^-a^-c^+)_3^4$ [11, 159, 160]. Further, Mishra *et al.* in 2011 used high-resolution neutron diffraction data to reinvestigate the complex structures of $NaNbO_3$ as a function of temperature. They reported several modifications in the temperature-dependent crystal structures of $NaNbO_3$ (see Fig. 1.12). Furthermore, Jiang *et al.* in 2013 analyzed the temperature-dependent long/short-range structure of $NaNbO_3$ using temperature-dependent neutron diffraction and pair distribution function data for 15 K $\leq T \leq$ 930 K [27]. The long-range crystal structure exhibits a series of structural phase transitions mentioned in the Table 1.6. On the other hand, short-range symmetry of $NaNbO_3$ was found to be rhombohedral with $R3c$ space group for $T <$ 490 K [27].

Table 1.6 Temperature-dependent evolution of long-range crystal structure of $NaNbO_3$ reported by Jiang *et al.* [27].

Temperature (K)	**Symmetry**	**Space Group**
15 K − 190 K	Orthorhombic + Rhombohedral	*Pbcm* + *R*3*c*
300 K − 490 K	Orthorhombic	*Pbcm*
600 K	Orthorhombic	*Pbnm*
700 K	Orthorhombic	*Pbnm* + *Cmcm*
770 K − 820 K	Orthorhombic	*Cmcm*
880 K	Tetragonal	$P4/mbm$
930 K	Cubic	$Pm\bar{3}m$

1.5.3 (K,Na)NbO_3

The solid solution of ferroelectric $KNbO_3$ with antiferroelectric $NaNbO_3$ *viz.*, $K_xNa_{(1-x)}NbO_3$ (KNN*x*) has been widely studied as a potential alternative to Pb-based materials [153, 161, 162]. $KNbO_3$ and $NaNbO_3$ have an orthorhombic crystal structure with *Amm*2 (Cell size: $1a_p \times \sqrt{2}b_p \times \sqrt{2}c_p$) and *Pbcm* (Cell size: $\sqrt{2}a_p \times \sqrt{2}b_p \times 4c_p$) space

groups respectively [8, 27, 160, 163]. As the potassium content (x) in KNNx increases, the antiferroelectric phase of $NaNbO_3$ (with *Pbcm* space group) transforms into ferroelectric phase of $KNbO_3$ (with *Amm*2 space group), *via* disappearance of superlattice reflections and modifications in the splitting/intensity of the main perovskite reflections (see Table 1.7). Consequently, the size and shape of the unit cell changes *via* antiferrodistorted ($q \neq 0$) and ferrodistorted ($q = 0$) structural phase transitions (see Table 1.7) [164, 165].

Table 1.7 Phase evolution of KNNx ceramics.

Potassium content (x)	**Tilt system**	**Phase (Space Group)**
$x = 0.00$	$(a^-a^-c^+)_1^2(a^-a^-c^-)_2^3(a^-a^-c^+)_3^4$	Orthorhombic (*Pbcm*) [11, 166]
$0.02 \leq x \leq 0.15$	$(a^-b^+c^-)$	Monoclinc (*Pm*) [164, 165]
$0.17 \leq x \leq 0.30$	$(a^-b^+c^0)$	Monoclinc (*Pm*) [164, 165]
$0.35 \leq x \leq 0.45$	$(a^0b^+c^0)$	Monoclinc (*Pm*) [164, 165]
$x = 0.50$	No tilts	Orthorhombic (*Amm*2) [55, 167] or Monoclinc (*Pm*) [56, 168]
$x = 1.00$	No tilts	Orthorhombic (*Amm*2) [157]

Moreover, the equimolar composition of $KNbO_3$ and $NaNbO_3$ *viz.*, KNN50 (x = 0.50) demonstrates a morphotropic phase boundary (MPB), resulting in high physical properties [115, 169]. Various authors have reported different crystal structures for KNN50 *viz.*, orthorhombic (with *Amm*2 space group [55, 115, 167, 170]) or monoclinic (with *Pm* space group [56, 115]). Orayech *et al.* in 2015 investigated the long-range crystal structure of KNN50 as a function of temperature using X-ray and neutron diffraction data, and demonstrated that KNN50 undergoes a series of structural phase transitions on heating *viz.*, $R3c \xrightarrow{\approx 135K} Amm2 \xrightarrow{\approx 465K} P4mm \xrightarrow{\approx 700K} Pm\bar{3}m$ [55]. Further, Kong *et al.* analyzed neutron diffraction data of KNN50 and reported another series of structural

phase transitions *viz.*, $Pm \xrightarrow{\approx 471K} P4mm \xrightarrow{\approx 674K} Pm\bar{3}m$ [56]. Furthermore, Kong *et al.* and Gupta *et al.* analyzed the short-range atomic ordering of KNN50 using Pair Distribution Function (PDF) data, and confirmed the presence of monoclinic symmetry with *Pm* space group stable for a wide temperature range. [56, 171].

1.5.4 (Ba,Sr)TiO_3

Ferroelectricity in perovskite oxides was first discovered in barium titanate ($BaTiO_3$) [14, 172]. $BaTiO_3$ exhibits a wide range of physical properties *viz.*, ferroelectricity, piezoelectricity, pyroelectricity, flexoelectricity, etc, making it a material of high interest to researchers [14, 172]. Owing to various physical properties, $BaTiO_3$ finds a wide range of applications *viz.*, multilayer ceramic capacitors (MLCCs), non-volatile ferroelectric memory, electro-optic devices, sensors, actuators, and energy harvesting systems [14, 172, 173, 174, 175]. Moreover, the eco-friendly nature of $BaTiO_3$ makes it a promising alternative to Pb-based ferroelectrics.

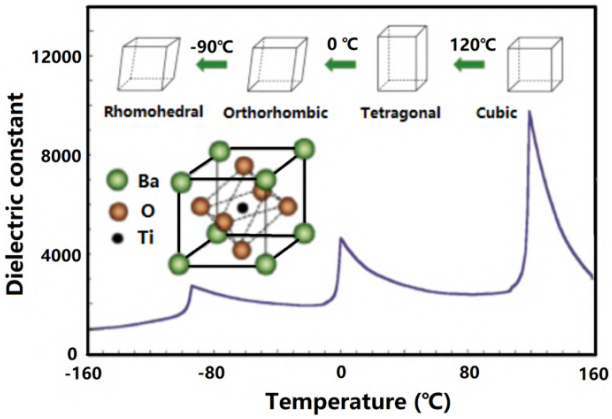

Fig. 1.13 Evolution of dielectric constant as a function of the temperature of $BaTiO_3$ [12].

Further, $BaTiO_3$ undergoes various long-range structural phase transitions on heating *viz.*, $R3m \xrightarrow{\approx 183K} Amm2 \xrightarrow{\approx 273K} P4mm \xrightarrow{\approx 393K} Pm\bar{3}m$ (see Fig. 1.13) [12]. Subsequently, at short ranges, a rhombohedral structure with $R3m$ space group is found to be stable for all the phases of $BaTiO_3$ [87].

On the other hand, Strontium titanate ($SrTiO_3$) is another perovskite oxide that exhibits fascinating temperature-dependent structural and dielectric properties. At room temperature, $SrTiO_3$ exhibits a cubic structure with $Pm\bar{3}m$ space group. On cooling, $SrTiO_3$ undergoes an antiferrodistortive (AFD) phase transition driven by octahedral tilting of TiO_6 octahedra at $\approx$ 105 K, resulting in a tetragonal phase with $I4/mcm$ space group [176, 177, 178, 179, 180]. Moreover, $SrTiO_3$ exhibits quantum paraelectric behavior, which inhibits ferroelectric displacements [177, 178, 179, 180]. Further, the temperature-dependent dielectric measurements of $SrTiO_3$ reveal a significant increase in the dielectric constant from $\approx$ 300 at room temperature to values exceeding 20,000 at cryogenic temperatures (see Fig. 1.14) [177, 178, 179, 180].

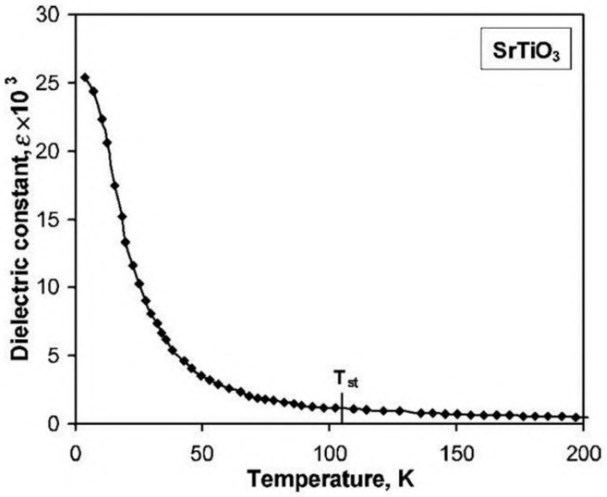

Fig. 1.14 Temperature-dependent evolution of dielectric constant of $SrTiO_3$. Here, T_{st} represents the transition temperature from cubic (Space Group: $Pm\bar{3}m$) to tetragonal (Space Group: $I4/mcm$) phase [13].

Furthermore, in order to enhance the physical properties of $BaTiO_3$, researchers have doped other elements at A/B-sites. Various researchers have doped strontium (Sr) at A-site of $BaTiO_3$ *i.e.*, $Ba_{(1-x)}Sr_xTiO_3$ to induce disorder/relaxor behavior. As Sr content increases, the structural phase transition temperatures (corresponding to paraelectric-ferroelectric transition and ferroelectric-ferroelectric transitions) shift towards low temperatures (see

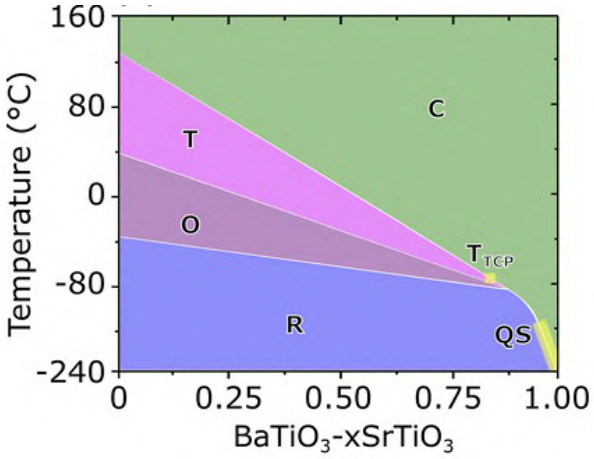

Fig. 1.15 Phase diagram of (Ba,Sr)TiO_3 [14].

Fig. 1.15) [14, 63, 65]. Subsequently, a cubic symmetry is found to be stable at room temperature for $x > 0.30$ [14]. Among various compositions (x) of $Ba_{(1-x)}Sr_xTiO_3$, the maximum dielectric constant is achieved for $x = 0.10$ (BST10). Moreover, BST10 exhibits all the structural phase transitions of $BaTiO_3$ but with a shift in structural phase transitions towards low temperatures [14, 63, 64, 65, 66, 181].

1.5.5 (K,Na,Ba)(Nb,Ti)O_3

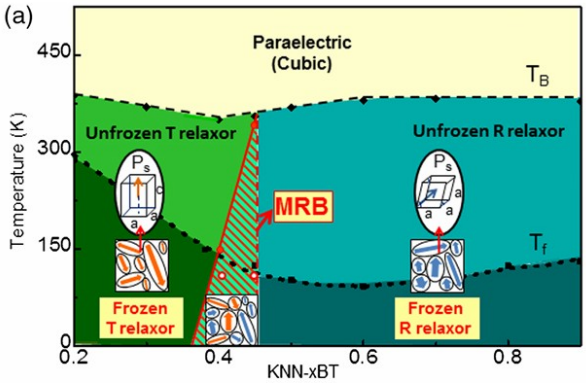

Fig. 1.16 Morphotropic Relaxor Boundary in KBTx system [15].

Owing to morphotropic phase boundary, KNN50 and its solid solutions are widely studied for its structure and properties. Recently, the solid solution of KNN50 and $BaTiO_3$

viz., (1-*x*)KNN50-*x*$BaTiO_3$ (*i.e.*, KBT*x*) has gained impetus due to the discovery of a new kind of morphotropic boundary referred to as morphotropic relaxor boundary (MRB) [15]. Here, MRB is defined as the composition-driven boundary with two polar phases coexisting at short ranges in an average cubic structure [15, 61, 182]. Yang *et al.* synthesized KBT*x* ceramics using solid-state reaction method and discovered an MRB in KBT*x* ceramics. They analyzed the long and short-range structures of KBT*x* ceramics for $0.20 \leq x \leq 0.90$ using X-ray diffraction, Raman scattering, and Transmission Electron Microscopy (TEM) data. X-ray diffraction data reveals a cubic symmetry at long ranges for $0.20 \leq x \leq 0.90$. On the other hand, temperature-dependent Raman scattering data uncovers the polar symmetries at short ranges *viz.*, tetragonal (for $0.20 \leq x \leq 0.40$), tetragonal and rhombohedral (for $x = 0.45$), and rhombohedral (for $0.45 < x \leq 0.90$) stable as a function of composition (see Fig. 1.16). Further evidence of local symmetries for $x = 0.30$ (tetragonal symmetry), $x = 0.45$ (tetragonal and rhombohedral symmetry), and $x = 0.60$ (rhombohedral symmetry) was given by using high-resolution transmission electron microscopy (HRTEM) and convergent beam electron diffraction (CBED). Furthermore, the physical properties *viz.*, electrostrain, and dielectric permittivity increase by ≈ 300 % and ≈ 150 % in the vicinity of MRB [15].

1.6 Organization of the thesis

The remainder of the thesis is structured to systematically explore the synthesis, structure, and associated physical properties of $K_{0.5}Na_{0.5}NbO_3$-based Pb-free perovskite materials.

Chapter 2 outlines the synthesis protocols used to prepare various compositions, along with a detailed description of the experimental techniques employed for structural and functional characterization.

Chapter 3 focuses on reinvestigation of the atomic-scale ordering in pure $K_{0.5}Na_{0.5}NbO_3$, analyzing both long- and short-range structures and their influence on ferroelectric properties.

Chapter 4 explores the structure and associated physical properties of the solid solutions based on $K_{0.5}Na_{0.5}NbO_3$, highlighting the emergence of long-range ferroelectricity originating from local polar order at short-range scales.

Chapter 5 reports the discovery of zero thermal expansion behavior in KNN50-based relaxor ferroelectrics and explains the underlying physical mechanisms responsible for ZTE in a Pb-free relaxor system.

Chapter 6 demonstrates the coexistence of distinct structural orderings across different length scales (long, intermediate, and short range) in the KNN50-based relaxor materials.

Chapter 7 investigates the role of multiple local symmetries within an average cubic structure (forming a morphotropic relaxor boundary (MRB)), in tuning thermal expansion in relaxor materials.

Finally, **Chapter 8** summarizes the major findings of the thesis and outlines potential future scope for research in the field of Pb-free perovskite materials.